JGR Space Physics

RESEARCH ARTICLE
10.1029/2019JA026610

Three-Dimensional Modeling of Callisto's Surface Sputtered Exosphere Environment

Audrey Vorburger[1], Martin Pfleger[2,3], Jesper Lindkvist[4,5], Mats Holmström[4], Helmut Lammer[3], Herbert I. M. Lichtenegger[3], André Galli[1], Martin Rubin[1], and Peter Wurz[1]

[1]Physikalisches Institut, University of Bern, Bern, Switzerland, [2]Institute for Chemical Engineering and Environmental Technology, Graz University of Technology, Graz, Austria, [3]Space Research Institute, Austrian Academy of Sciences, Graz, Austria, [4]Swedish Institute of Space Physics, Kiruna, Sweden, [5]Department of Physics, Umeå University, Umeå, Sweden

Abstract We study the release of various elements from Callisto's surface into its exosphere by plasma sputtering. The cold Jovian plasma is simulated with a 3-D plasma-planetary interaction hybrid model, which produces 2-D surface precipitation maps for magnetospheric H^+, O^+, O^{++}, and S^{++}. For the hot Jovian plasma, we assume isotropic precipitation onto the complete spherical surface. Two scenarios are investigated: one where no ionospheric shielding takes place and accordingly full plasma penetration is implemented (*no-ionosphere* scenario) and one where an ionosphere lets virtually none of the cold plasma but all of the hot plasma reach Callisto's surface (*ionosphere* scenario). In the 3-D exosphere model, neutral particles are sputtered from the surface and followed on their individual trajectories. The 3-D density profiles show that whereas in the no-ionosphere scenario the ram direction is favored, the ionosphere scenario produces almost uniform density profiles. In addition, the density profiles in the ionosphere scenario are reduced by a factor of ~2.5 with respect to the no-ionosphere scenario. We find that the Neutral Gas and Ion Mass Spectrometer, which is part of the Particle Environment Package on board the JUpiter ICy moons Explorer mission, will be able to detect the different sputter populations from Callisto's icy surface and the major sputter populations from Callisto's nonicy surface. The chemical composition of Callisto's exosphere can be directly linked to the chemical composition of its surface and will offer us information not only on Callisto's formation scenario but also on the building blocks of the Jupiter system.

Key Points:
- We investigate Callisto's surface sputtered exosphere; two cases are investigated: one with an ionosphere present and one with no ionosphere
- The case where no ionosphere is present produces an asymmetric exosphere, with favoring of the ram direction (direction of plasma arrival)
- With an ionosphere present, the exosphere is almost uniform, and densities are ~2.5 times lower than in the case without an ionosphere

Correspondence to:
A. Vorburger,
vorburger@space.unibe.ch

Citation:
Vorburger, A., Pfleger, M., Lindkvist, J., Holmström, M., Lammer, H., & Lichtenegger, H. I. M., et al. (2019). Three-dimensional modeling of Callisto's surface sputtered exosphere environment. *Journal of Geophysical Research: Space Physics*, *124*. https://doi.org/10.1029/2019JA026610

Received 12 FEB 2019
Accepted 10 JUL 2019
Accepted article online 31 JUL 2019

1. Introduction

It is well established that Callisto's surface consists of both ice and mineral components (Greeley et al., 2000; Kuskov & Kronrod, 2005), though what their volume mixing ratio is and to what degree the moon is differentiated still remains unclear (e.g., Nagel et al., 2004, and references therein).

The chemical ice composition of Jupiter's large satellites depends mainly on the early thermodynamic conditions within the Jovian environment prior to their accretion (Alibert, Mordasini, Benz, & Winisdoerffer 2005; Alibert, Mousis, & Benz, 2005; Mousis & Alibert, 2006). Two formation scenarios that result in two distinct ice surface compositions are often associated with the icy moons. One of these compositions represents an oxidizing state, which is based on the assumption that the building blocks of the Galilean satellites were formed in the protosolar nebula. The second composition represents a reducing state, based on the assumption that the satellites accreted from building blocks that condensed in Jupiter's subnebula. Measuring the chemical ice compositions of the Jovian satellites would bring important constraints on both their formation conditions and on the thermodynamic conditions that took place in the protosolar nebula during the formation of the giant planets. ESA's JUpiter ICy moons Explorer (JUICE; Grasset et al., 2013) with its various instruments will help us to distinguish between the different formation scenarios.

To date, only CO_2 was directly measured in Callisto's exosphere (Carlson, 1999). Other species, including CO, O_2, O, and C, have been inferred indirectly from measurements or have been modeled to match measurements (e.g., Cunningham et al., 2015; Kliore et al., 2002; Strobel et al., 2002). We thus still know only very little about Callisto's atmosphere.

Concerning surface composition, two distinct absorption bands in Callisto's reflectance spectra were attributed to the presence of CO_2 and SO_2 molecules (Carlson et al., 1996; McCord et al., 1998). Both species seem to be distributed asymmetrically over the surface of Callisto, where the trailing hemisphere (subplasma hemisphere) is more enriched in CO_2 and the leading hemisphere (plasma opposing hemisphere) is more enriched in SO_2 (Hibbitts et al., 2000). Atmospheric CO_2 column densities at the dayside have been estimated by Carlson (1999) to be about 8×10^{14} cm^{-2}. Calvin and Clark (1991) presented a compilation of spectral observations of Callisto's surface from 0.2 to 4 μm, exhibiting properties that are similar to those of phyllosilicate minerals commonly found in carbonaceous chondrite meteorites. For that reason Cl chondrites are often chosen to represent Callisto's mineral component, matching these observations well.

Upper hybrid resonance measurements obtained by the plasma wave instrument on board of Galileo revealed peak electron densities near Callisto's orbit of about 400 cm^{-3} (Gurnett et al., 2000). Electron measurements were also carried out by the Galileo radio occultation instrument (Kliore et al., 2002), but their derived electron densities could not be reproduced solely by ionization of the observed CO_2 atmosphere (Carlson, 1999). Therefore, Kliore et al. (2002) proposed an O_2 component in addition to a tenuous CO_2 gas envelope with an inferred O_2 column density of (3–4) $\times 10^{16}$ cm^{-2}. Recently, Cunningham et al. (2015) inferred from observations of doublet and triplet lines of atomic oxygen the existence of an O_2-dominated "atmosphere" related to Callisto's leading/Jupiter-facing hemisphere by using the far-ultraviolet sensitivity of the Cosmic Origins Spectrograph on board of the Hubble Space Telescope. From the Hubble Space Telescope observations, these authors infer a leading hemisphere extended molecular oxygen corona with an O_2 column density of 3.4×10^{15} cm^{-2} (Cunningham et al., 2015). These authors mention that the highly variable O_2 density could be an order of magnitude larger at the trailing hemisphere, which does agree well with Chapman-type ionospheric layers and inferred column densities obtained by Kliore et al. (2002) for the Callisto C22 and C23 flybys. Furthermore, the aperture-filling emissions implied that there is also an extended atomic oxygen corona present with an exobase density of up to $\approx 10^4$ cm^{-3} (where exobase denotes the base altitude of the exosphere). These findings are consistent with measurements of the atomic oxygen surface column density for which an upper limit of about 2.5×10^{13} cm^{-2} was found (Strobel et al., 2002).

Depending on the plasma environment in Jupiter's magnetosphere, environmental conditions, and geographical surface areas on Callisto, the exobase altitude may be located at the satellite's surface or may move atop a collision-dominated atmosphere envelope tens kilometers above the surface. That this variation exists can also be inferred from Galileo radio occultation measurements (Kliore et al., 2002). It was found that Callisto can have a substantial ionosphere (i.e., C22 and C23 flyby) with a Chapman-type layer when the trailing hemisphere (which correlates with the magnetospheric ramside) is illuminated by sunlight (Kliore et al., 2002). The C20 flyby, which had a similar configuration as C22 and C23, though, yielded electron densities three to four times lower. This lower electron density indicates that during flyby C20 the density of the neutral gas envelope was lower than during the flybys C22 and C23. During the ramside/nightside flyby C9, where the leading hemisphere was illuminated by sunlight, no ionosphere was discernible (Kliore et al., 2002). This led Kliore et al. (2002) to speculate that impact of energetic ions from the magnetosphere of Jupiter and photoionization by the sunlight might be needed to create an ionosphere. This disagrees with the C3 and C10 flybys, though, where Callisto's position with respect to Jupiter and the Sun was almost identical to the C9 flyby, but where the flyby was on Callisto's dayside rather than on the nightside. During both flybys, a factor 100–1,000 increase in plasma density was observed (Gurnett et al., 1997, 2000).

The Neutral and Ion Mass spectrometer (NIM), which is part of the Particle Environment Package (PEP) (Barabash et al., 2013) on board JUICE, will be able to shed light onto Callisto's formation scenario and provide information on the building blocks of the Jupiter system by measuring the neutral and ion composition of Callisto's (and the other Galilean moons') exosphere (see also Vorburger et al., 2015). NIM is able to determine the exospheric chemical composition with high mass resolution and unprecedented sensitivity: The mass resolution is $M/\Delta M > 1{,}100$ in the mass range 1–1,000 u, and NIM's energy range is 0–5 eV for neutrals and <10 eV for ions. The detection level for neutral gas is 1×10^{-16} mbar for a 5-s accumulation time, which corresponds to a particle density of about 1 cm^{-3}.

Under the assumption that sputtering releases all species present on the surface stoichiometrically into the exosphere (Plainaki et al., 2018), this process allows us to derive the chemical composition of the surface of Callisto from NIM measurements during the flybys. In the present study we thus focus on species that

are released from Callisto's surface by plasma sputtering and investigate with a 3-D model how the different species are distributed geographically around the satellite.

In section 2 we present the applied 3-D hybrid plasma interaction model that produces ion precipitation maps, the implemented ice and mineral surface compositions, the sputter yield computations, and the 3-D exosphere model. In section 3 we present the results of our simulations for two different scenarios: one where no ionosphere is present and the magnetospheric plasma reaches Callisto's surface almost unhindered (called *no-ionosphere* scenario) and one where an ionosphere shields the surface almost completely from the thermal magnetospheric plasma and only energetic ions (also refereed to as radiation) reach the surface (called *ionosphere* scenario). In section 4 we discuss the relevance of our results for the planned PEP/NIM measurements during the JUICE mission. The paper ends with a brief conclusion given in section 5.

2. Description of Plasma and Exosphere Model

The aim of this work is to model Callisto's surface sputtered exosphere in 3-D. First, we apply a 3-D plasma-planetary-interaction hybrid model that produces 2-D ion precipitation maps of magnetospheric H^+, O^+, O^{++}, and S^{++} onto the satellite's surface. The obtained 2-D precipitation maps are then used to calculate the corresponding latitude- and longitude-dependent sputter fluxes by multiplying the precipitation maps with the energy dependent sputter yields. This result in turn serves as an input for the exosphere model, where we compute for each surface species the resulting exospheric density profile in 3-D. The different models and assumptions are described in the subsections below.

2.1. Coordinate System and Simulation Domain

The coordinate system we use is called "Satellite Centered Phi-B Coordinates," a coordinate system often used to model magnetic field interactions with satellites. The coordinate system is centered in the middle of Callisto. The $+x$ axis is in the direction of the plasma flow. The z axis is defined such that the x-z plane contains the Jovian magnetic field B_0. The y axis is normal to B_0 and x, that is, completes the right-hand system. Note that depending on the location of Callisto with respect to Jupiter's magnetic equatorial plane, the magnetic field might point anywhere from perpendicular to the magnetic equatorial plane to toward Jupiter. Since we are interested in plasma interaction with the satellite, though, in this study Callisto is located in the center of the plasma sheet and the magnetic field points parallel to Jupiter's spin axis. The convective electric field is given by $E_0 = -u \times B_0$, where u is the plasma bulk velocity. Note that in this configuration, the undisturbed convective electric field will always be in the $-y$ direction.

The simulation domain is divided into a Cartesian grid with cubic cells of the size $\Delta x = r_C/16$, where r_C is the radius of Callisto, that is, 2,410.3 km. We use nine macroparticles per cell as the initial condition and include periodic boundary conditions.

When the simulation is initiated, the ions (macroparticles) are evenly distributed everywhere outside Callisto, according to a Maxwellian distribution. Also, the magnetic field is homogeneous everywhere and equal to the given external field. We model Callisto as an inert object; all particles are absorbed by the surface.

2.2. Hybrid Plasma Interaction Model

The hybrid plasma interaction model used herein has previously been applied to solar wind interaction studies with the Moon (Holmström et al., 2012) and to plasma interaction studies with Callisto (Lindkvist et al., 2015). In this study we use hybrid simulations similar to Lindkvist et al. (2015) where Callisto is modeled as a conductive body without atmosphere and without ionosphere. In the hybrid approximation, ions are treated as particles, and electrons are treated as a massless fluid. Figure 1 shows the flow of the magnetospheric plasma in the hybrid model, where the total ion densities are shown in panels a and b and the mean ion velocity is shown in panels c and d for both the XY and XZ planes. The results are taken after 110 s of simulation time. Further details on the hybrid model used here (including the discretization) can be found in Holmström (2011), Holmström and Barabash (2011), and Holmström et al. (2012). In this study, the hybrid plasma interaction model has only been used to model the cold, thermal part of the magnetospheric plasma. We produce individual surface precipitation maps for each ion species of the cold plasma, which corotates with Jupiter's magnetic field and most of which arrives from Callisto's ram direction.

In the wake of Callisto to the Jovian magnetospheric plasma flow, the plasma densities of the cold, thermal plasma can be low, or even zero. In such regions of low ion charge density the hybrid solver can have

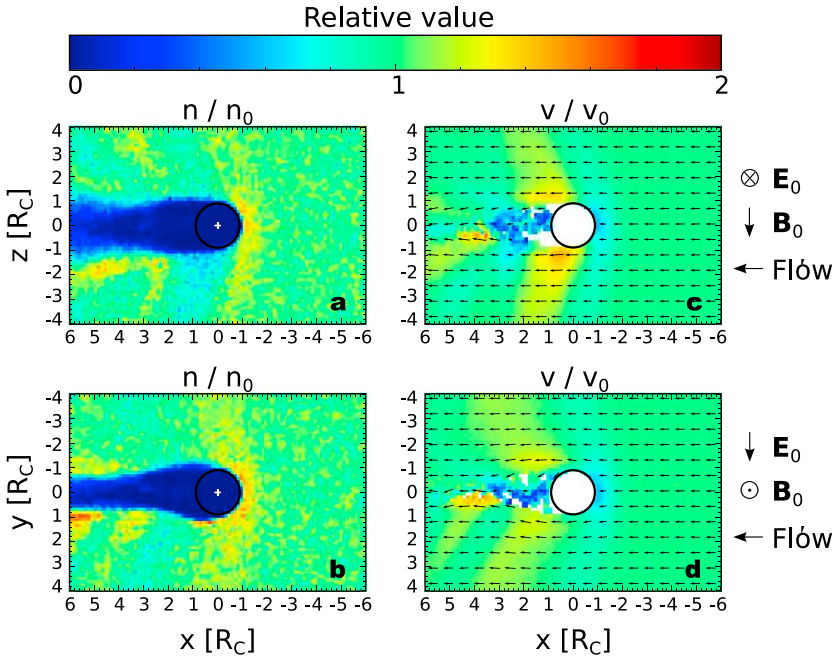

Figure 1. Magnetospheric ion flow around Callisto in the hybrid model for two geometric planes: *XZ* for panels a and c and *XY* for panels b and d. Shown in color is the total ion number densities (a and b) and the mean ion speed (c and d). The vector field in c and d shows the direction of the mean ion velocity. The axes are given in Callisto radii, R_C = 2,410.3 km.

numerical problems due to large gradients in the electric field leading to high accelerations of ions resulting in numerical instabilities. We handle such regions of low ion charge density by solving a magnetic diffusion equation. The magnetic diffusion is also solved inside the obstacle to the plasma flow, in this case inside the spherical inner boundary of the moon's surface (Holmström, 2013).

For the hot, energetic plasma, which, due to the particles' large gyro-radii, is almost isotropic, we implement uniform plasma arrival onto the complete spherical surface as described below.

2.3. Plasma Parameters

Jupiter's magnetospheric plasma comprises two populations: The cold, thermal plasma and the hot, energetic plasma (sometimes also referred to as radiation).

The flow of the cold Jovian magnetospheric plasma passing Callisto at ≈27 R_J (with R_J being Jupiter's radius or 69,911 km) is sub-Alfvénic or almost sub-Alfvénic (Neubauer, 1998). The total magnetospheric plasma density at Callisto's orbit fluctuates between ≈0.01 and 1 cm^{-3} (Kivelson et al., 2004; Neubauer, 1998). We assume for the ambient magnetospheric plasma parameters at Callisto's orbit an average number density of 0.1 cm^{-3} (Kivelson et al., 2004), a bulk ion velocity of $v_{ion} \approx 192$ km/s (Kivelson et al., 2004), an ion temperature of $T_{ion} = 200$ eV (Neubauer, 1998), and an electron temperature of $T_{ele} = 100$ eV (Neubauer, 1998). The corresponding gyro-radii amount to ~(60–900) km, depending on the particle mass and charge. We simulated 1-D sputtered density profiles within an ion bulk velocity ranging between 132 and 252 km/s and found that the used average bulk velocity resembles the complete velocity range well. The most abundant magnetospheric ion at Callisto's orbit is O^+ (Bagenal et al., 1992; McNutt et al., 1981). Bagenal et al. (2015) presented plasma conditions at Europa's orbit. We assume that the plasma composition is similar at Callisto's orbit and implement ion abundance ratios for $O^+ : S^{++} : H^+ : O^{++}$ as 15 : 10.5 : 6 : 4, with oxygen clearly dominating.

The energetic population of the Jovian plasma is presented in Figure 3 of Cooper et al. (2001). The hot plasma particles' energy ranges from 10 keV to 100 MeV, with a characteristic energy of ≈100 keV and a temperature of ~20 keV. This results in gyro-radii between 1.3×10^3 and 5.2×10^3 km, values of the same order as Callisto's radius (~2,410 km). Peak fluxes are on the order of 10^{10} m^{-2}/s. Integrated over energy and solid angle, and considering shielding by the moon, we obtain energetic particle fluxes onto the surface of

$\sim 2 \times 10^6$ cm^{-2}/s, almost the exact same value as the one obtained for the cold population. We implemented the relative abundance of H^+, O^{n+}, and S^{n+} according to Figure 3 in Cooper et al. (2001) as $O^{n+} : S^{n+} : H^+ = 6 : 3 : 1$. Note that these abundances were derived from flux averages over 5 hr as Callisto moved in and out of the local magnetospheric current sheet and could be variable on shorter time scales, for example, as Callisto crosses through the center of the current sheet.

The induced magnetic dipole in the simulation has the same magnitude found in the C3 flyby made by the Galileo spacecraft, which is discussed in Lindkvist et al. (2015), but with an orientation directly opposing the background magnetic field ($+\hat{z}$). The Jovian magnetic field vector is $\boldsymbol{B}_0 = -35\hat{z}$ nT. Because the precipitating ion flux on Callisto's surface is directly connected to the flux of the sputtered species, the ion flux regulates the sputtered density profile. Therefore, one can use the modeled density profiles and adjust them to different ion flux values.

2.4. Ionospheric Shielding

Observations show that Callisto has a highly variable ionosphere, as discussed in section 1. Strobel et al. (2002) implemented a cylindrical symmetric ionosphere and computed that less than 0.07% of the impinging cold plasma will reach the surface. In a simulation of Io's interaction with the Io plasma torus, Saur et al. (1999) showed that as the plasma is diverted, it is also slowed down. Assuming that the cold plasma is slowed down by the same degree as it is shielded, the cold plasma bulk velocity decreases from ≈192 km/s to ≈134 m/s when an ionosphere of the given density is present. With water being bound to icy surfaces with a binding energy of ∼0.45 eV (Famá et al., 2008), the corresponding ion kinetic energy of 0.0001 to 0.003 eV is not high enough to liberate icy surface water molecules anymore. When we thus study sputtering in the case of an ionosphere being present, we only implement sputtering by hot plasma ions but not by cold plasma ions. Note, though, that whereas the slowed cold plasma particles do not contribute to the sputter yield anymore, they are (to 0.07% of the upstream value) still available for atmospheric interaction processes (i.e., loss processes; see below).

We decided to present two cases in accordance to the Galileo observations during the C3 and C10 versus the C9 flybys discussed above: one labeled ionosphere, where an ionosphere lets all of the hot plasma but only 0.07% of the cold plasma pass, and where no cold plasma sputtering yet cold plasma interaction takes place, and one labeled no ionosphere, where no ionospheric shielding takes place.

2.5. Magnetospheric Ion Precipitation Maps

In the hybrid model, the ion number density and mean ion fluxes are stored to a grid with the given cell size. We define the precipitating ion flux as the component of the mean ion flux that is antiparallel to the surface normal. Then we choose points on the surface separated by an angle in both longitude and latitude, given by the angular size of half a cell at the equator. At each point on the surface, we interpolate a value for the chosen parameter (ion number density or precipitating flux) using the cells around it. This is done by creating an imaginary cell with its center at the point of interest and then sum the contributions from the enclosed simulation cells. Since the cell size, $\Delta x = r_C/16$, is not infinitely small, the interpolation will result in a value at a mean altitude of ≈36 km.

Figure 2 shows the impinging fluxes of cold H^+, O^+, O^{++}, and S^{++} used in the no-ionosphere case. One can see that the flux is higher for O ions than for S and H ions. The majority of magnetospheric ions precipitate onto the surface over the ramside, which is the trailing hemisphere that faces Jupiter's corotating magnetospheric plasma flow. In addition, the antiramside also experiences some ion fluxes, but the flux values are much lower than on the ramside. Fluxes of ions precipitating onto the surface as function of latitude and longitude are used as input parameters for the surface interaction and sputter yield modeling described below.

2.6. Surface Composition and Sputter Modeling

For this study we assume similar surface compositions and use the ion velocity-dependent sputter yields as presented in Vorburger et al. (2015).

In our model runs we assume for the icy surface composition the aforementioned oxidizing state, which is based on the assumption that the building blocks of Callisto were formed in the protosolar nebula. The composition belonging to the oxidizing state can be found in Table 1 of Vorburger et al. (2015). The advantage of taking the oxidizing state rather than the reducing state is that it includes all major volatile compounds. A comparison with the reducing case is simple, since one can just ignore the CO_xH_y molecules and instead

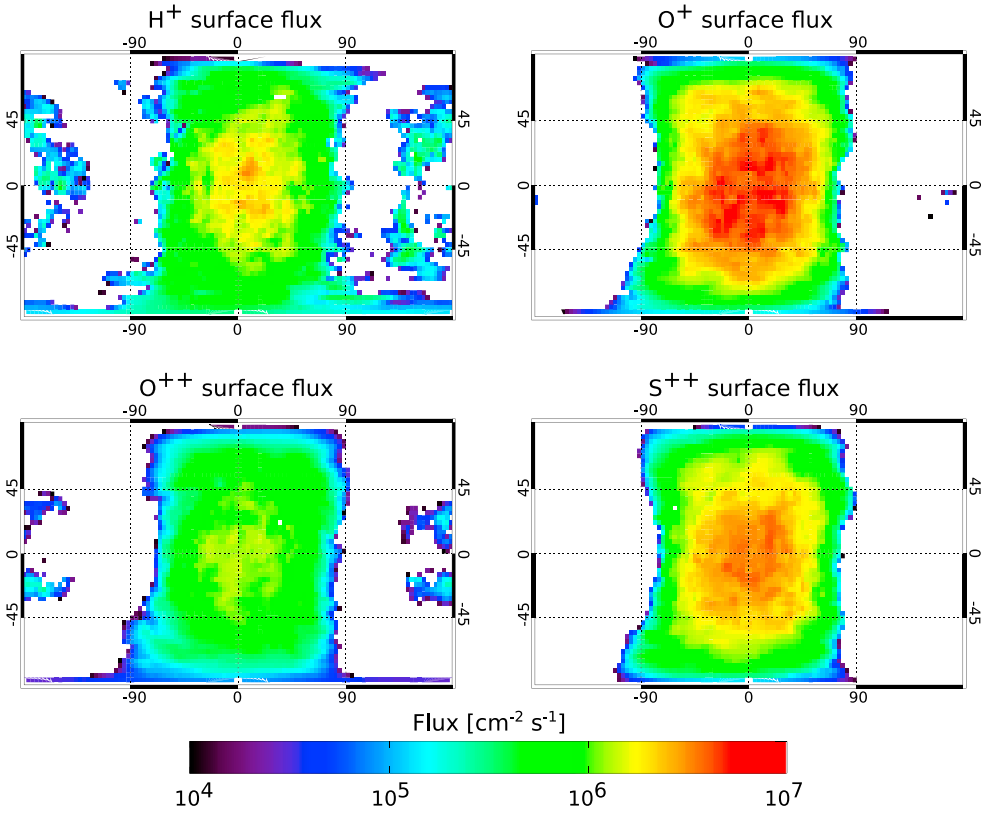

Figure 2. Maps of precipitating cold magnetospheric H^+, O^+, O^{++}, and S^{++} ions onto Callisto's surface in units of $cm^{-2}\ s^{-1}$ used in the no-ionosphere case. The hemisphere facing Jupiter's corotating magnetospheric plasma flow (ramside) lies in the center of the precipitation maps; positive latitudes correspond to Callisto's northern hemisphere, and positive longitudes represent the eastern hemisphere.

increase the CH_4 and NH_3 fractions. For the nonice compositions we study the compositions of typical LL chondrites for Mg and of typical CI chondrites for Fe (see Table 2 in Vorburger et al., 2015).

The sputter yields for ices have been calculated based on the experimental results from Shi et al. (1995) and the extension by Famá et al. (2008) and Galli et al. (2018). For both sputtering from icy and nonicy surfaces we assume that the ion charge state does not influence the sputter yield (Galli et al., 2017; Muntean et al., 2016). Shi et al. (1995) found that for solar wind protons the sputter yield of water ice is about a factor 10 higher than for sputtering of mineral grains. Thus, similar as in Vorburger et al. (2015), electronic excitations related to icy surfaces, which results in much higher sputter yields, are considered for icy surfaces. For the sputter yield of O_2, which is a radiolysis product of H_2O, we used the sputter yield of H_2O and scaled it to the abundance of O_2 expected to be present in plasma processed water ice. (For more information see section 3.3.1 and Table 2 in Vorburger & Wurz, 2018.) Thermal desorption and thermal accommodation has not been considered in this paper but will be presented in a follow-up paper. The sputter yields for minerals have been determined with the Stopping and Range of Ions in Matter code, which calculates ion interactions with matter (http://www.srim.org; Ziegler, 2004). The Stopping and Range of Ions in Matter tool uses a Monte Carlo simulation method for the calculation of the binary collisions between an impacting ion and atoms on the surface for a given chemical composition of the surface. Inputs are the sputter agent's mass, energy, and angle of incidence. For the surface the input parameters are the present atoms' weight percentages, the thickness of the simulated layer, and the layer's density.

The total sputter yield Y_i of species i is calculated by $Y_i = x^{H^+} Y_i^{H^+} + x^{O^{n+}} Y_i^{O^{n+}} + x^{S^{n+}} Y_i^{S^{n+}}$, where x^{H^+}, $x^{O^{n+}}$, and $x^{S^{n+}}$ are the fractions of H^+, O^{n+}, and S^{n+} ions in Jupiter's corotating magnetospheric plasma flow, while $Y_i^{H^+}$, $Y_i^{O^{n+}}$, and $Y_i^{S^{n+}}$ are the sputter yields of species i caused by the precipitating ions.

2.7. Three-Dimensional Exosphere Modeling

The sputter yields of the released chemical species are then used as the basic input into the 3-D exosphere model. In this model, the trajectories of a large amount of particles are computed independently (i.e., the model is collision free) ab initio, that is, starting at the surface. Each sputtered particle starts its trajectory at the exobase (which in this case is assumed to be Callisto's surface), with an energy sampled randomly from the energy distribution function for sputtered particles:

$$f(E) = \frac{6E_b}{3 - 8\sqrt{E_b/E_c}} \frac{E}{(E + E_b)^3} \left(1 - \sqrt{\frac{E + E_b}{E_c}}\right), \tag{1}$$

where E_b is the surface binding energy and E_c is the maximum energy that can possibly be transferred in a binary collision between the impacting particle and the surface atom. Typical energies of sputtered particles are on the order of 0.1 eV. The particles' ejection angles are obtained by randomly sampling a cosine function for the polar angle and a uniform distribution for the azimuth angle. Three-dimensional trajectories are computed until the particles either leave the calculation domain, get ionized, are fragmented, or fall back to the surface. Particles that return to the surface are assumed to be completely sticking. More details of the 3-D exosphere model are given in Pfleger et al. (2015).

The sputter rate Q_{sp} in units of per second of the particles that are generated in a surface element is calculated by

$$Q_{\mathrm{sp}} = \int Y \cdot J dA, \tag{2}$$

with A the area related to a surface element, Y the sputter yield, and J the impinging plasma flux.

A total of about 10^6 pseudo-particles equally distributed over Callisto's surface are generated, where the surface production rate $Q_{\mathrm{sp}}^{\mathrm{p}}$ assigned to each pseudo-particle can be written as

$$Q_{\mathrm{sp}}^{\mathrm{p}} = \frac{Q_{\mathrm{sp}}}{N}, \tag{3}$$

where N is the number of pseudo-particles of the considered surface element. The simulation domain reaches from the surface up to 2.5×10^4 km or 10.37 Callisto radii (half of Callisto's Hill radius). Particles that move beyond this altitude or impinge at the surface are considered as lost.

In addition to atmospheric escape and surface sticking, we consider ionization and dissociation as loss processes. Several different particle populations can ionize or dissociate neutral particles in Callisto's exosphere. Ionization is only effective in a limited energy range, usually a few tens of electron volts to a few tens of kiloelectron volts. We accordingly only consider ionization by solar photons, cold plasma electrons, cold plasma ions, and ionospheric O_2^+ (the most abundant ion in the ionosphere). For dissociation we consider solar photons and cold plasma electrons, the most efficient dissociation agents.

For loss processes involving photons we use values given at 1 AU by Huebner et al. (1992) and http://phidrates.space.swri.edu and scale them to Callisto's distance to the Sun. To determine the atmospheric loss rate by electron and ion impact, we multiply the respective particle fluxes with the interaction specific cross-sections. The cold plasma electron flux is taken as the product of the electron density and the electron thermal velocity based on $T_{ele} = 100$ eV, whereas the cold plasma ion flux is obtained directly from our hybrid model. Accordingly, the electron flux is the same in the no-ionosphere and in the ionosphere case, whereas cold plasma ion ionization becomes ineffective in the ionosphere case due to the ions' low energy. With the neutral O_2 flux being the source for the ionospheric O_2^+ flux, we try to estimate the ionospheric O_2^+ flux based on the neutral sputtered O_2 flux. To this end, we model the neutral O_2 flux and multiply it with the ionization fraction, that is, the number of particles that were ionized during our Monte Carlo simulations (≈0.04%). The obtained O_2^+ particle flux of 1×10^{10} cm^{-2}/s is about 2 orders of magnitude higher than the O_2^+ flux that was similarly computed for Europa (Vorburger & Wurz, 2018). This agrees well with the neutral O_2 density being also approximately 100 times denser on Callisto than on Europa. The cross-sections were assembled from Garrett et al. (1985), Freund et al. (1990), Tawara et al. (1990), McCallion et al. (1992), Kanik et al. (1993), Straub et al. (1996), Boivin and Srivastava (1998), McGrath and Johnson (1989), Deutsch et al. (2000), Johnson et al. (2002), Luna et al. (2005), Riahi et al. (2006), and McConkey et al. (2008) for an electron energy of ~100 eV and an ion energy of a few kiloelectron volts.

Table 1
Molecular Reaction Rates for O_2 and Mg

	No ionosphere			Ionosphere		
process	σ (10^{-16} cm^2)	J (cm^{-2} s^{-1})	r (10^{-6} s^{-1})	σ (10^{-16} cm^2)	J (cm^{-2} s^{-1})	r (10^{-6} s^{-1})
O_2						
hν dissociation			0.15			0.15
e$^-$ dissociation	0.33	J_{e^-} = 8.9e07	0.0003	0.33	J_{e^-} = 8.9e07	0.0003
hν ionization			0.02			0.02
e$^-$ ionization	1.56	J_{e^-} = 8.9e07	0.014	1.56	J_{e^-} = 8.9e07	0.014
Plasma chex	15	$J_{i^{n+}}$ = 1.9e06	0.003			
Ionosph. chex				14	$J_{O_2^+}$ = 1.0e10	14.00
Total			0.19			14.18
Mg						
hν ionization			0.02			0.02
e$^-$ ionization	2.4	J_{e^-} = 8.9e07	0.021	2.4	J_{e^-} = 8.9e07	0.021
Plasma chex	<20	$J_{i^{n+}}$ = 1.9e06	0.004			
Ionosph. chex				86	$J_{O_2^+}$ = 1.0e10	86.00
Total			0.045			86.04

Note. "Chex" refers to charge exchange.

Table 1 lists ionization and fragmentation loss rates computed for O_2 and Mg for the no-ionosphere case and for the ionosphere case separately. As one can see from this table, if an ionosphere of the calculated density is present, the charge exchange between the ionospheric ions and the neutral particles dominates the neutrals' loss rates by orders of magnitude. If no ionosphere is present, the loss rate is mainly determined by the photon-dissociation rate. We only performed these detailed considerations for neutral O_2 and Mg but use the reported rates for all icy and nonicy species. Cross-sections of processes involving other neutral species will be different from the ones reported for O_2 and Mg, but on the same order of magnitude. Considering the overall uncertainties in cross-sections and particle fluxes, we feel confident that the loss rates reported for O_2 and Mg in Table 1 are also applicable for other neutral species.

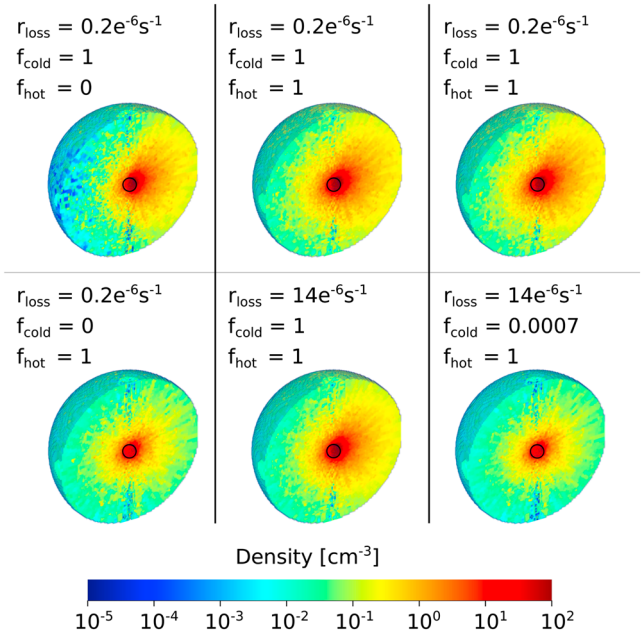

Figure 3. Number density cuts in units of per cubic centimeter for surface sputtered H_2O. The magnetospheric ramside is on the right-hand side, and $-\boldsymbol{B}_0$ points upward. The left two panels show the individual sputter contributions by the cold and the hot plasma for a fixed loss rate (0.2×10^{-6} s^{-1}). The middle two panels show the density profiles for full plasma penetration for two different loss rates. The right two panels show the computed H_2O density profiles for the no-ionosphere and the ionosphere cases. The simulation domain extends between the surface and an altitude of 25,000 km or 10.37 Callisto radii.

3. Results and Discussion

Figure 3 shows he density profiles of H_2O (the most abundant ice species) sputtered from Callisto's surface for four sensitivity cases (nonrealistic scenarios) and two realistic scenarios. The left side panels present the individual contributions of the cold and the hot plasma for a fixed loss rate of 0.2×10^{-6} s^{-1} (no-ionosphere loss rate), the central two panels show the effect of two different loss rates (0.2×10^{-6} s^{-1} from the no-ionosphere scenario and 14×10^{-6} s^{-1} from the ionosphere scenario) for full plasma penetration, and the right two panels show the resulting total density distributions for the two scenarios no ionosphere/ionosphere (with the right plasma penetration and loss rates implemented). Note that the artifacts in the pole directions are a result of the grid discretization.

The comparison between the two plasma populations (left side panels) shows that the cold plasma and the hot plasma contribute about equally to the overall H_2O density profiles. The cold plasma creates, as expected, a density profile with a longitude and latitude dependency, where most particles are sputtered in the the direction of plasma arrival, that is,

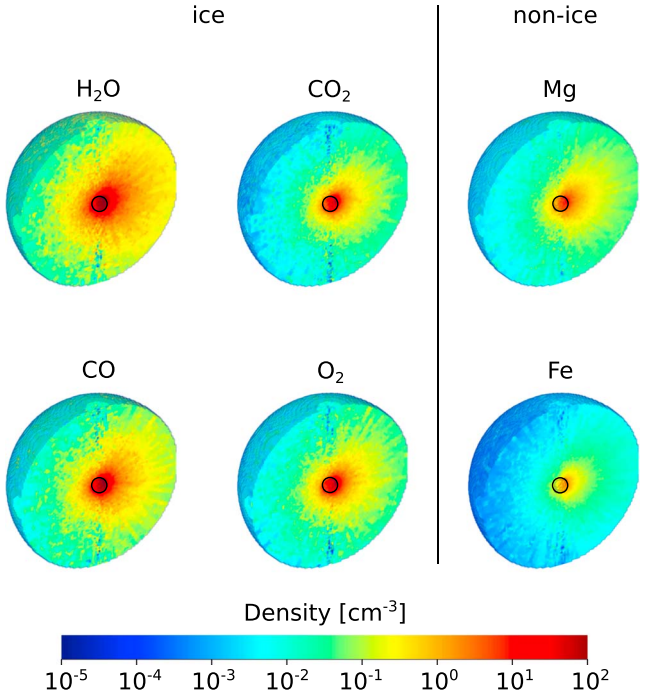

Figure 4. Number density cuts in units of per cubic centimeter for H_2O, CO_2, CO, and O_2 sputtered from an oxidizing icy surface, Mg sputtered from a LL-type chondritic nonicy surface, and Fe sputtered from a CI chondritic nonicy surface for the no-ionosphere case. The magnetospheric ramside is on the right-hand side, and $-B_0$ points upward. The simulation domain extends between the surface and an altitude of 25,000 km or 10.37 Callisto radii.

the trailing side of Callisto. The hot plasma contribution, on the other hand, creates an almost uniform exosphere.

The two different loss rates computed for the two different scenarios do not seem to have a large impact on the density profiles of the neutral exosphere. One does observe a slightly more rapid density decrease in the case of the higher loss rate (e.g., the orange color reaches less far out), but with the ionization rate being small compared to the average particle flight time, the difference in the two profiles is minor.

The density profiles for the two scenarios no ionosphere/ionosphere do not show any surprises either. For the no-ionosphere scenario, we implement full plasma penetration and apply the lower loss rate of 0.2×10^{-6} s^{-1}. For the ionosphere scenario we use 100% of the hot plasma ions but none of the cold plasma ions for sputtering and apply the higher loss rate of 14×10^{-6} s^{-1} (i.e., 0.07% of the cold plasma is still available for charge exchange). The no-ionosphere exosphere density profile contains ~2.5 times as many particles than the ionosphere profile. The exosphere is less uniform in the no-ionosphere case, with more particles sputtered in the direction of plasma arrival than in other directions (north/south, leading side of Callisto). The ionosphere density profile is almost identical to the hot plasma density profile, with the only difference being a slightly steeper decrease in density with altitude due to the higher loss rate caused by ionospheric charge exchange processes.

In the following two subsections, we will present the density profiles corresponding to the two scenarios no ionosphere and ionosphere separately.

3.1. Without Ionosphere

Figure 4 shows the modeled number density distributions for H_2O, CO_2, CO, and O_2 sputtered from an icy surface (oxidizing case), and for Mg and Fe sputtered from a nonice surface, with a composition of LL and CI chondrite, for the scenario where 100% of both the hot and the cold plasma reach Callisto's surface (no ionosphere).

The average global number densities of sputtered H_2O molecules are ≈110 cm^{-3} near the surface, ≈32 cm^{-3} at 1,000 km, and ≈1 cm^{-3} at 10,000 km. The densities on the ramside hemisphere are ≈1.5 times higher than the global average, whereas the densities on the antiramside hemisphere are ≈2 times lower than the global average. The average global number densities of sputtered CO_2, CO, and O_2 are ≈8, 2, and 5 times lower, respectively, compared to the global H_2O densities. The density profiles for the nonice components are ≈9 times lower for Mg and ≈57 times lower for Fe than for H_2O. Those lower nonice density profiles result from the lower sputter yields for nonice materials than for icy materials. In addition, Mg is about three times more abundant in LL chondrites than Fe is in CI chondrites and weighs less than half as much as Fe, so the difference in scale height between the two nonice density profiles is also well understood.

Overall, the density profiles of all sputtered species in the no-ionosphere case exhibit the same characteristics as the density profile of H_2O: a denser exosphere on the ramside and less density toward the poles and on the antiramside.

The 1-D simulations presented in Figure 3 of Vorburger et al. (2015) are ≈3 to 4 times lower than the densities presented in this work. It is noteworthy that while the model applied in the Vorburger et al. (2015) study is quite similar to the model used herein, there are, besides the dimensionality, two major differences. First of all, Vorburger et al. (2015) only considered the cold plasma distribution, whereas in this work both the cold and the hot plasma contributions are considered. This already explains a factor ≈1.5 difference between the two analyses. Second, Vorburger et al. (2015) approximated the cold plasma by three mono-energetic ion fluxes (one for H^+, one for O^+, and one for S^{++}), while we use the precipitation maps created by our hybrid model. These maps are not only more accurate but also slightly higher at the subplasma point than

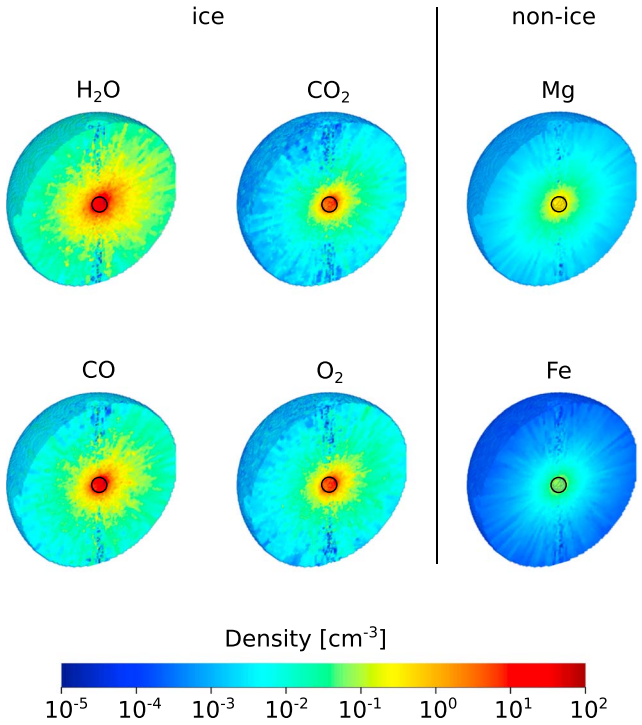

Figure 5. Number density cuts in units of per cubic centimeter for H_2O, CO_2, CO, and O_2 sputtered from an oxidizing icy surface, Mg sputtered from a LL-type chondritic nonicy surface, and Fe sputtered from a CI chondritic nonicy surface for the ionosphere case. The magnetospheric ramside is on the right-hand side, and $-B_0$ points upward. The simulation domain extends between the surface and an altitude of 25,000 km or 10.37 Callisto radii.

the averages used in the Vorburger et al. (2015) study. Overall, the herein presented 3-D profiles thus agree very well with the 1-D profiles computed previously.

3.2. With Ionosphere

Figure 5 shows the modeled number densities for H_2O, CO_2, CO, and O_2 sputtered from an icy surface (oxidizing case), and for Mg and Fe sputtered from a nonice surface composition (LL and CI chondrite) for the scenario where all of the hot plasma but only 0.07% of the cold plasma ions reaches Callisto's surface (ionosphere). Remember that whereas the cold plasma does not contribute to the sputter yield (due to the plasma's low velocity), it is still available for atmospheric loss processes.

The global H_2O number densities are $\approx$76 cm^{-3} near the surface, $\approx$21 cm^{-3} at 1,000 km, and $\approx$0.53 cm^{-3} at 10,000 km. They are thus, for the ionospheric density assumed, $\sim$2 times lower than in the no-ionosphere scenario. Note that, as mentioned in section 1, the ionosphere is highly variable, which makes this factor also highly variable. The average global number densities of sputtered CO_2, CO, and O_2 are also $\approx$8, 2, and 5 times lower, respectively. The ratios are thus very similar to the no-ionosphere case. The density profiles for the nonice components are $\approx$22 and 108 times lower for Mg and Fe than for H_2O. These ratios are larger than the ratios of the no-ionosphere scenario, because mineral sputtering is mainly triggered by cold plasma ions.

Overall, the density profiles associated with the ionosphere scenario are $\approx$2.5 times lower for icy constituents and $\approx$5.5 times lower for nonicy constituents than in the no-ionosphere scenario. They are almost uniform, with only a slight favoring of the ram direction.

4. PEP/NIM Measurements

JUICE, ESA's first Jupiter-dedicated mission, is planned for launch in 2022 and will arrive at Jupiter in 2029, where it will spend at least 3 years performing detailed observations of Jupiter and its largest icy moons. Several Callisto flybys will provide the JUICE scientific instruments with the opportunity to closely investigate Jupiter's second-largest moon. NIM is a neutral gas and ionospheric ion mass spectrometer designed to investigate the chemical composition of the exospheres of the Galilean moons. The instrument is characterized by a high mass resolution of $M/\Delta M > 1{,}100$ and an unprecedented sensitivity with a detection level of 1×10^{-16} mbar ($\sim$1 cm^{-3}) for a 5-s accumulation time.

With its high sensitivity, NIM will be able to detect all water ice-related species modeled herein, with H_2O surpassing NIM's instrument background as far out as 10^4 km above the surface. CO and O_2 will become measurable at a few thousand kilometers, whereas the least abundant species modeled, CO_2, will be detectable at $\approx 10^3$ km. Determination of the amount of CO, CO_2, and CH_4 (a molecule highly abundant in the reducing case) in Callisto's exosphere during a Callisto flyby is thus well feasible. With the exosphere representing the surface composition more or less stoichiometrically (Plainaki et al., 2018), knowledge of the chemical composition of Callisto's exosphere will allow us to directly deduce the chemical composition of Callisto's surface and will thus help us to gain insight into Callisto's formation scenario.

Since the nonice-related species are much less abundant than the ice-related species, they pose a challenge concerning measurability. In the study presented herein, out of the two minerals investigated only Mg surpasses NIM's instrument background, and only at closest approach. The detection limit for a given species depends on the orbital characteristics (flyby speed and altitude), possible integration time, and the scale height of the sputtered particles. Since the neutral particle densities and scale heights are dependent on plasma conditions (more energetic plasma ions impose more energy onto the surface particles and higher plasma fluxes result in higher neutral fluxes), more favorable measurement conditions (but also less

favorable measurement conditions) can be expected. In fact, the profiles presented herein correspond to an average ion particle density of 0.1 cm^{-3}, whereas, according to Kivelson et al. (2004), the ion particle density ranges from 0.01 to 0.5 cm^{-3}, and the ion bulk velocity ranges from 122 to 272 km/s while 192 km/s was used herein.

5. Conclusion

The release of various surface elements caused by plasma sputtering from an assumed icy and a nonicy surface has been studied. The results of the 3-D plasma-planetary interaction hybrid model are used as input for a sputter-3-D exosphere code that has been used to derive exosphere density profiles and distributions as a function of Callisto's latitude and longitude. We have analyzed two different scenarios, one where no ionospheric shielding takes place (no-ionosphere scenario) and one where an ionosphere only lets 0.07% of the cold plasma, but all of the hot plasma reach Callisto's surface (ionosphere scenario). In the second scenario, due to the associated cold plasma retardation, no cold plasma ion sputtering takes place. These particles are, though, still available for interaction loss processes. The no-ionosphere density profiles show a clear variation with longitude and latitude, with most particles being released in the ram direction (direction of cold plasma arrival). The ionosphere density profiles are almost uniform, and about 2.5 times lower than the no-ionosphere density profiles. The nonicy density profiles are lower than the icy density profiles by a factor of ≈10 to 100 but exhibit the same geometric characteristics as the icy density profiles.

NIM will be able detect most major ice and the most abundant nonice surface constituents. Ice species will be detectable as early as 10^4 km above the surface, whereas nonice species will only be revealed close to the closest approach (200 km). Measurements of the chemical composition of Callisto's exosphere are directly applicable to Callisto's surface and will shed light onto Callisto's formation scenario and provide information on the building blocks of the Jovian system.

Acknowledgments
Data used to create Figures 1–5 presented in this paper can be retrieved from Vorburger (2019). A. Vorburger, A. Galli, M. Rubin, and P. Wurz gratefully acknowledge the financial support by the Swiss National Science Foundation. This work was conducted using resources provided by the Swedish National Infrastructure for Computing (SNIC) at the High Performance Computing Center North (HPC2N), Umeå University, Sweden. The hybrid model used in this work was in part developed by the DOE NNSA-ASC OASCR Flash Center at the University of Chicago. Jesper Lindkvist is funded by the Swedish National Space Board (SNSB). M. Pfleger, H. Lammer and H. I. M. Lichtenegger acknowledge the support by the Austrian Research Foundation FWF NFN Subproject S11607-N16 "Particle/Radiative Interactions with Upper Atmospheres of Planetary Bodies Under Extreme Stellar Conditions."

References

Alibert, Y., Mordasini, C., Benz, W., & Winisdoerffer, C. (2005). Models of giant planet formation with migration and disc evolution. *Astronomy & Astrophysics*, *434*, 343–353.

Alibert, Y., Mousis, O., & Benz, W. (2005). Modeling the Jovian subnebula: I. Thermodynamic conditions and migration of proto-satellites. *Astronomy & Astrophysics*, *439*, 1205–1213.

Bagenal, F., Shemansky, D. E., Jr, R. L. M., Schreier, R., & Eviatar, A. (1992). The abundance of O^{++} in the Jovian magnetosphere. *Geophysical Research Letters*, *19*, 79–82.

Bagenal, F., Sidrow, E., Wilson, R. J., Cassidy, T. A., Dols, V., Crary, F. J., et al. (2015). Plasma conditions at Europa's orbit. *Icarus*, *261*, 1–13. https://doi.org/10.1016/j.icarus.2015.07.036

Barabash, S., Wurz, P., Brandt, P., Wieser, M., Holmström, M., Futaana, Y., et al. (2013). Particle Environment Package (PEP), European Planetary Science Congress 2013, held 8-13 September in London, UK, 8.

Boivin, R. F., & Srivastava, S. K. (1998). Electron-impact ionization of Mg. *Journal of Physics B Atomic Molecular Physics*, *31*, 2381–2394. https://doi.org/10.1088/0953-4075/31/10/024

Calvin, W. M., & Clark, R. N. (1991). Modeling the reflectance spectrum of Callisto 0.25 to 4.1 μm. *Icarus*, *89*, 305–317.

Carlson, R. W. (1999). A Tenuous Carbon Dioxide Atmosphere on Jupiter's Moon Callisto. *Science*, *283*, 820–821. https://doi.org/10.1126/science.283.5403.820

Carlson, R., Smythe, W., Baines, K., Barbinis, E., Becker, K., Burns, R., et al. (1996). Near-infrared spectroscopy and spectral mapping of Jupiter and the Galilean satellites: Results from Galileo's initial orbit. *Science*, *274*, 385–388.

Cooper, J. F., Johnson, R. E., Mauk, B. H., Garrett, H. B., & Gehrels, N. (2001). Energetic ion and electron irradiation of the icy Galilean satellites. *Icarus*, *149*, 133–159. https://doi.org/10.1006/icar.2000.6498

Cunningham, N. J., Spencer, J. R., Feldman, P. D., Strobel, D. F., France, K., & Osterman, S. N. (2015). Detection of Callisto's oxygen atmosphere with the Hubble Space Telescope. *Icarus*, *254*, 178–189. https://doi.org/10.1016/j.icarus.2015.03.021

Deutsch, H., Becker, K., Matt, S., & Mark¨, T. D. (2000). Theoretical determination of absolute electron-impact ionization cross sections of molecules. *International Journal of Mass Spectrometry*, *197*, 37–69. https://doi.org/10.1016/S1387-3806(99)00257-2

Famá, M., Shi, J., & Baragiola, R. A. (2008). Sputtering of ice by low-energy ions. *Surface Science*, *602*, 156–161. https://doi.org/10.1016/j.susc.2007.10.002

Freund, R. S., Wetzel, R. C., Shul, R. J., & Hayes, T. R. (1990). Cross-section measurements for electron-impact ionization of atoms. *Physical Review A*, *41*, 3575–3595. https://doi.org/10.1103/PhysRevA.41.3575

Galli, A., Vorburger, A., Wurz, P., Cerubini, R., & Tulej, M. (2018). First experimental data of sulphur ions sputtering water ice. *Icarus*, *312*, 1–6. https://doi.org/10.1016/j.icarus.2018.04.029

Galli, A., Vorburger, A., Wurz, P., & Tulej, M. (2017). Sputtering of water ice films: A re-assessment with singly and doubly charged oxygen and argon ions, molecular oxygen, and electrons. *Icarus*, *291*, 36–45. https://doi.org/10.1016/j.icarus.2017.03.018

Garrett, B. C., Redmon, L. T., McCurdy, C. W., & Redmon, M. J. (1985). Electronic excitation and dissociation of O2 and S2 by electron impact. *Physical Review A*, *32*(6), 3366–3375.

Grasset, O., Dougherty, M. K., Coustenis, A., Bunce, E. J., Erd, C., Titov, D., et al. (2013). JUpiter ICy moons Explorer (JUICE): An ESA mission to orbit Ganymede and to characterise the Jupiter system. *Planetary and Space Science*, *78*, 1–21. https://doi.org/10.1016/j.pss.2012.12.002

Greeley, R., Klemaszewski, J. E., Wagner, R., & the Galileo Imaging Team (2000). Galileo views of the geology of Callisto. *Planetary and Space Science*, *48*, 829–853.

Gurnett, D. A., Kurth, W. S., Roux, A., & Bolton, S. J. (1997). Absence of a magnetic-field signature in plasma-wave observations at Callisto. *Nature*, *387*, 261–262. https://doi.org/10.1038/387261a0

Gurnett, D. A., Persoon, A. M., Kurth, W. S., Roux, A., & Bolton, S. J. (2000). Plasma densities in the vicinity of Callisto from Galileo plasma wave observations. *Geophysical Research Letters*, *27*, 1867–1870. https://doi.org/10.1029/2000GL003751

Hibbitts, C. A., McCord, T. B., & Hansen, G. B. (2000). Distributions of CO2 and SO2 on the surface of Callisto. *Journal of Geophysical Research*, *105*, 22,541–22,557. https://doi.org/10.1029/1999JE001101

Holmstrom¨, M., Fatemi, S., Futaana, Y., & Nilsson, H. (2012). The interaction between the Moon and the solar wind. *Earth, Planets, and Space*, *64*, 237–245. https://doi.org/10.5047/eps.2011.06.040

Holmström, M. (2011). An energy conserving parallel hybrid plasma solver. In N. V. Pogorelov, E. Audit, & G. P. Zank (Eds.), *5th international conference of numerical modeling of space plasma flows (astronum 2010)* (Vol. 444, pp. 211). San Francisco, CA: Astronomical Society of the Pacific.

Holmström, M. (2013). Handling vacuum regions in a hybrid plasma solver. In N. V. Pogorelov, E. Audit, & G. P. Zank (Eds.), *Numerical modeling of space plasma flows (astronum2012)* (Vol. 474, pp. 202). San Francisco, CA: Astronomical Society of the Pacific.

Holmström, M., & Barabash, S. (2011). Hybrid Simulations of the Callisto-Magnetosphere interaction. In *EPSC-DPS Joint Meeting 2011* (pp. 689). Nantes, France.

Huebner, W. F., Keady, J. J., & Lyon, S. P. (1992). Solar photo rates for planetary atmospheres and atmospheric pollutants. *Astrophysics and Space Science*, *195*(1), 1–294.

Johnson, R. E., Liu, M., & Tully, C. (2002). Collisional dissociation cross sections for O+O_2, CO and N_2, O_2+O_2, N+N_2, and N_2+N_2. *Planetary and Space Science*, *50*, 123–128. https://doi.org/10.1016/S0032-0633(01)00067-8

Kanik, I., Trajmar, S., & Nickel, J. C. (1993). Total electron scattering and electronic state excitations cross sections for O2, CO, and CH4. *Journal of Geophysical Research*, *98*, 7447–7460. https://doi.org/10.1029/92JE02811

Kivelson, M. G., Bagenal, F., Kurth, W. S., Neubauer, F. M., Paranicas, C., & Saur, J. (2004). *Jupiter: The planet, satellites and magnetosphere*, vol. 1, pp. 513–536: Cambridge University Press.

Kliore, A. J., Anabtawi, A., Herrera, R. G., Asmar, S. W., Nagy, A. F., Hinson, D. P., & Flasar, F. M. (2002). Ionosphere of Callisto from Galileo radio occultation observations. *Journal of Geophysical Research*, *107*(A11), 1407. https://doi.org/10.1029/2002JA009365

Kuskov, O. L., & Kronrod, V. A. (2005). Internal structure of Europa and Callisto. *Icarus*, *177*, 550–569. https://doi.org/10.1016/j.icarus.2005.04.014

Lindkvist, J., Holmstrom¨, M., Khurana, K. K., Fatemi, S., & Barabash, S. (2015). Callisto plasma interactions: Hybrid modeling including induction by a subsurface ocean. *Journal of Geophysical Research: Space Physics*, *120*, 4877–4889. https://doi.org/10.1002/2015JA021212

Luna, H., McGrath, C., Shah, M. B., Johnson, R. E., Liu, M., Latimer, C. J., & Montenegro, E. C. (2005). Dissociative charge exchange and ionization of O_2 by fast H^+ and O^+ Ions: Energetic ion interactions in Europa's oxygen atmosphere and neutral torus. *The Astronomical Journal*, *628*, 1086–1096. https://doi.org/10.1086/431140

McCallion, P., Shah, M. B., & Gilbody, H. B. (1992). Multiple ionization of magnesium by electron impact. *Journal of Physics B: Atomic, Molecular, and Optical Physics*, *25*(5), 1051–1060.

McConkey, J. W., Malone, C. P., Johnson, P. V., Winstead, C., McKoy, V., & Kanik, I. (2008). Electron impact dissociation of oxygen-containing molecules—A critical review. *Physics Reports*, *466*, 1–103. https://doi.org/10.1016/j.physrep.2008.05.001

McCord, T. B., Hansen, G. B., Clark, R. N., Martin, P. D., Hibbitts, C. A., Fanale, F. P., et al. (1998). Non-water-ice constituents in the surface material of the icy Galilean satellites from the Galileo near-infrared mapping spectrometer investigation. *Journal of Geophysical Research*, *103*, 8603–8626. https://doi.org/10.1029/98JE00788

McGrath, M. A., & Johnson, R. E. (1989). Charge exchange cross sections for the Io plasma torus. *Journal of Geophysical Research*, *94*, 2677–2683. https://doi.org/10.1029/JA094iA03p02677

McNutt, R. L., Belcher, J. W., & Bridge, H. S. (1981). Positive ion observations in the middle magnetosphere of Jupiter. *Journal of Geophysical Research*, *86*, 8319–8342. https://doi.org/10.1029/JA086iA10p08319

Mousis, O., & Alibert, Y. (2006). Modeling the Jovian subnebula—II. Composition of regular satellite ices. *Astronomy & Astrophysics*, *448*(L7), 771–778. https://doi.org/10.1051/0004-6361:20053211

Muntean, E. A., Lacerda, P., Field, T. A., Fitzsimmons, A., Fraser, W. C., Hunniford, A. C., & McCullough, R. W. (2016). A laboratory study of water ice erosion by low-energy ions. *Monthly Notices of the Royal Astronomical Society*, *462*, 3361–3367.

Nagel, K., Breuer, D., & Spohn, T. (2004). A model for the interior structure, evolution, and differentiation of Callisto. *Icarus*, *169*, 402–412. https://doi.org/10.1016/j.icarus.2003.12.019

Neubauer, F. M. (1998). The sub-Alfvenic interaction of the Galilean satellites with the Jovian magnetosphere. *Journal of Geophysical Research*, *103*, 19,843–19,866. https://doi.org/10.1029/97JE03370

Pfleger, M., Lichtenegger, H. I. M., Wurz, P., Lammer, H., Kallio, E., Alho, M., et al. (2015). 3D-modeling of Mercury's solar wind sputtered surface-exosphere environment. *Planetary and Space Science*, *115*, 90–101. https://doi.org/10.1016/j.pss.2015.04.016

Plainaki, C., Cassidy, T. A., Shematovich, V. I., Milillo, A., Wurz, P., Vorburger, A., et al. (2018). Towards a global unified model of Europa's tenuous atmosphere. *Space Science Reviews*, *214*, 40. https://doi.org/10.1007/s11214-018-0469-6

Riahi, R., Teulet, P., Ben Lakhdar, Z., & Gleizes, A. (2006). Cross-section and rate coefficient calculation for electron impact excitation, ionisation and dissociation of H_2 and OH molecules. *European Physical Journal D*, *40*, 223–230. https://doi.org/10.1140/epjd/e2006-00159-2

Saur, J., Neubauer, F. M., Strobel, D. F., & Summers, M. E. (1999). Three-dimensional plasma simulation of Io's interaction with the Io plasma torus: Asymmetric plasma flow. *Journal of Geophysical Research*, *104*, 25,105–25,126. https://doi.org/10.1029/1999JA900304

Shi, M., Baragiola, R. A., Grosjean, D. E., Johnson, R. E., Jurac, S., & Schou, J. (1995). Sputtering of water ice surfaces and the production of extended neutral atmospheres. *Journal of Geophysical Research*, *100*, 26387.

Straub, H. C., Renault, P., Lindsay, B. G., Smith, K. A., & Stebbings, R. F. (1996). Absolute partial cross sections for electron-impact ionization of H_2, N_2, and O_2 from threshold to 1000 eV. *Physical Review A*, *54*, 2146–2153. https://doi.org/10.1103/PhysRevA.54.2146

Strobel, D. F., Saur, J., Feldman, P. D., & McGrath, M. A. (2002). Hubble Space Telescope space telescope imaging spectograph search for an atmosphere on Callisto: A Jovian unipolar inductor. *Astronomy Journal*, *581*, 51–54.

Tawara, H., Itikawa, Y., Nishimura, H., & Yoshino, M. (1990). Cross sections and related data for electron collisions with hydrogen molecules and molecular ions. *Journal of Physical and Chemical Reference Data*, *19*, 617–636. https://doi.org/10.1063/1.555856

Vorburger, A. (2019). Callisto 3D Exosphere. osf.io/kuzdf. OSF.

Vorburger, A., & Wurz, P. (2018). Europa's ice-related atmosphere: The sputter contribution. *Icarus*, *311*, 135–145. https://doi.org/10.1016/j.icarus.2018.03.022

Vorburger, A., Wurz, P., Lammer, H., Barabash, S., & Mousis, O. (2015). Monte-Carlo simulation of Callisto's exosphere. *Icarus*, *262*, 14–29. https://doi.org/10.1016/j.icarus.2015.07.035
Ziegler, J. (2004). SRIM-2003, Nucl. Instrum. Methods B Nucl. instrum. methods b.